

## Mesoscale simulations of the rheology of filled styrene–butadiene compounds

Fitzgerald, Barry W.; den Otter, Wouter K.; Luding, Stefan; Briels, Wim J.

**DOI**

[10.1002/mats.201800014](https://doi.org/10.1002/mats.201800014)

**Publication date**

2018

**Document Version**

Final published version

**Published in**

Macromolecular Theory and Simulations

**Citation (APA)**

Fitzgerald, B. W., den Otter, W. K., Luding, S., & Briels, W. J. (2018). Mesoscale simulations of the rheology of filled styrene–butadiene compounds. *Macromolecular Theory and Simulations*, 27(5), Article 1800014. <https://doi.org/10.1002/mats.201800014>

**Important note**

To cite this publication, please use the final published version (if applicable). Please check the document version above.

**Copyright**

Other than for strictly personal use, it is not permitted to download, forward or distribute the text or part of it, without the consent of the author(s) and/or copyright holder(s), unless the work is under an open content license such as Creative Commons.

**Takedown policy**

Please contact us and provide details if you believe this document breaches copyrights. We will remove access to the work immediately and investigate your claim.



# Mesoscale Simulations of the Rheology of Filled Styrene–Butadiene Compounds

Barry W. Fitzgerald,\* Wouter K. den Otter, Stefan Luding, and Wim J. Briels

The ability of a highly coarse-grained polymer model is explored to simulate the impact of carbon black (CB) filler concentration on the rheological properties of unvulcanized styrene–butadiene melts—an intermediate stage in the production of styrene–butadiene rubber (SBR) commonly used in tyres. Responsive particle dynamics (RaPiD), previously used to study dilute polymeric systems, models entire polymers as single particles interacting through a combination of conservative interactions and transient entanglement-mimicking forces. The simulation parameters are tuned to the linear rheology of the unfilled melt, as measured using a rubber process analyzer (RPA). For the filled compounds, only the interaction between the polymers and fillers is varied. On top of excluded volume interactions, a slight attraction ( $\approx 0.1 k_B T$ ) between polymers and fillers is required to attain agreement with RPA measurements. The physical origins of the small strength of this interaction are discussed. This method offers potential for future numerical investigations of filled melts.

particles, the properties of rubber can be significantly altered, producing compounds of practical importance for many applications such as automobiles, aircraft and in the biomedical industry. There are a number of filler particle options available for filled elastomer compounds. Automobile tyres are filled with carbon black<sup>[1–8]</sup> or silica.<sup>[4,5,9–16]</sup> For most applications, carbon black or silica tend to be exclusively employed, although mixtures of these materials have also been used in order to exploit the advantages of both filler types.<sup>[10,17]</sup> Clay offers an alternative filler option, but its reinforcing capability is poor in comparison to both carbon black and silica.<sup>[18]</sup> Graphite, graphene, and carbon nanotubes have also been considered as alternative filler particles<sup>[15,19,20]</sup> given the environmental<sup>[21]</sup> and health<sup>[22]</sup> repercussions of using carbon black in tyre products.

## 1. Introduction

Rubber, both natural and synthetic, is soft and fragile and therefore unsuitable for applications where materials resistant to abrasion are required. With crosslinking and the addition of filler

While the goal is to improve some properties, there are a number of negative effects that may develop in crosslinked filled elastomer matrices, due in part to the presence of filler particles, such as the Payne effect<sup>[23]</sup> and the Mullins effect.<sup>[24,25]</sup> In the former, the storage modulus decreases when the sample is subject to oscillatory perturbations of increasing strain amplitude; the severity of the effect depends on the amount of filler in the material. The Mullins effect is the softening of the stress–strain curve below the all-time maximum deformation, relative to the first deformation to that maximum.<sup>[24,26,27]</sup> Unlike the Payne effect, the Mullins effect also occurs in elastomers without filler. The inclusion of filler particles in elastomers can also lead to a shift in the glass transition temperature near the particles<sup>[28,29]</sup> where the polymer matrix is glassy in nature.<sup>[30]</sup> The physisorption of polymers by the fillers promotes the development of a network connecting the fillers, the so-called bound rubber layer, the elastomer that is nonextractable from a filled elastomer even with a good solvent such as toluene.<sup>[31–34]</sup> Of particular relevance to this study is the material strengthening of filled compounds in comparison to unfilled elastomers.<sup>[1,2,7,8,28,35,36]</sup> In fact, material reinforcement in a filled crosslinked compound is due to both the vulcanization of the rubber and the filler particle inclusion.<sup>[1,32]</sup>

In this study, we will focus on the filler particle concentration and its effect on the mechanical properties of unvulcanized filled elastomers using both experimental and computational approaches. We are specifically interested in the mechanical strengthening, as characterized by the shear relaxation modulus, that results from the inclusion of varying amounts of carbon black filler in high temperature flowing

Dr. B. W. Fitzgerald, Dr. W. K. den Otter, Prof. S. Luding  
Multi Scale Mechanics  
Faculty of Engineering Technology  
University of Twente

P.O. Box 217, 7500 AE Enschede, The Netherlands  
E-mail: b.fitzgerald@tudelft.nl, barry.w.fitzgerald@gmail.com

Dr. B. W. Fitzgerald, Dr. W. K. den Otter, Prof. W. J. Briels  
Computational BioPhysics  
Faculty of Science and Technology  
University of Twente

P.O. Box 217, 7500 AE Enschede, The Netherlands

Dr. B. W. Fitzgerald, Dr. W. K. den Otter, Prof. S. Luding, Prof. W. J. Briels  
MESA+ Institute for Nanotechnology  
University of Twente

P.O. Box 217, 7500 AE Enschede, The Netherlands

Dr. B. W. Fitzgerald  
Process & Energy Department  
Delft University of Technology  
Leeghwaterstraat 39, 2628 CB Delft, The Netherlands  
Prof. W. J. Briels

Forschungszentrum Jülich  
ICS 3, D-52425 Jülich, Germany

The ORCID identification number(s) for the author(s) of this article can be found under <https://doi.org/10.1002/mats.201800014>.

DOI: 10.1002/mats.201800014

unvulcanized elastomer matrices as encountered in the production process of tyre rubber. In particular we are interested in the viscoelastic response for timescales up to 1 s, a timescale over which the compound does not yet undergo significant relaxation when subject to processing. The mechanical behavior and inelastic features of filled elastomers have previously been studied numerically using continuum models,<sup>[27,29,37–39]</sup> microscopic molecular dynamics (MD)<sup>[40–44]</sup> and mesoscopic dissipative particle dynamics (DPD).<sup>[2,28,45,46]</sup> Due to the extensive time and length scales that are needed to resolve the macroscopic mechanical properties, some degree of coarse graining is a necessity. One such approach explicitly models only the filler particles while the rubber–filler interactions are included through micromechanical considerations<sup>[2]</sup> or in the interaction potential for the rubber itself.<sup>[28]</sup> In this feasibility study, we apply, for the first time, the highly coarse-grained approach known as responsive particle dynamics (RaPiD)<sup>[47–51]</sup> to simulate filled SBR compounds. In RaPiD, each elastomer or polymer is represented as a point particle with the dynamical effects of the eliminated degrees of freedom retained to describe the viscoelastic response within and between particles. Using the RaPiD approach, we explicitly model all interaction types, i.e., polymer–polymer, polymer–filler, and filler–filler in the compound. In particular we will explore the effect of varying the interaction potential between the filler particles and the surrounding elastomer on the mechanical properties.

This paper is arranged as follows. In Section 2 we describe the materials used in this study, i.e., the styrene–butadiene melt and the carbon black, and the experimental apparatus, a rubber process analyzer (RPA), used to measure the viscoelastic response of the samples. In Section 3 we outline the RaPiD algorithm. Comparison of the experimental and computational data is presented in Section 4.1 for the pure elastomer. In Section 4.2, we study the impact of the carbon black filler concentration on the mechanical properties of filled rubber compounds in both experiments and simulations. For the simulations, we vary the filler–rubber interaction potential to ascertain its relevance in strengthening the filled compounds. We end in Section 5 with a discussion of the simulation results and an outlook.

## 2. Experimental Section

### 2.1. Samples

The elastomer used in this study was a random non-crosslinked copolymer of styrene and 1,3-butadiene (SBR) rubber with a molecular weight  $M_w$  in the range  $370 \text{ kg mol}^{-1}$ , a polydispersity index (PDI) of  $\approx 2.1$ , and a glass transition temperature  $T_g \approx 253 \text{ K}$ . In measurements of the elastomer in tetrahydrofuran (THF) solution using gel permeation chromatography (GPC), the radius of gyration,  $R_g$ , of the polymers varied between 10 and 20 nm, with a small amount having an  $R_g$  up to 40 nm. Under melt conditions, the size of the polymers was expected to be slightly smaller than in THF solution. Unfilled samples consisted of the SBR only without additives such as aromatic oils, hydrocarbon resins, plasticizers, and liquid or rubber soluble chemicals.

For the filled SBR compounds, CORAX N660 carbon black (CB) supplied by Orion Engineered Carbons as was used as the

filler component. The primary N660 particle was roughly spherical with a mean radius of  $\approx 31.5 \text{ nm}$ . During production, however, these particles tend to fuse together to form “aggregates,” where the mean diameter of the aggregates is  $\approx 85 \text{ nm}$ , which in turn can coalesce to form larger filler “agglomerates.” Five batches of filled SBR samples with differing filler concentration were prepared, as qualified by the parts per hundred rubber (phr), or the filler mass added to every 100 g of SBR. All batches were prepared subject to the same mixing procedure on a Brabender 350 S using the following protocol. First, the elastomer was loaded into the mixer. After 90 s half of the carbon black was added and a further 60 s later the second half of the carbon black filler was loaded. After 3 min 30 s the mixtures were subjected to a frequency sweep protocol, before dumping of the mixed compounds after 6 min. All mixtures were then processed on a two-roll mill. The mass of each unvulcanized sheet was  $\approx 280 \text{ g}$ . Each filled sample consisted of two components only—SBR polymer and the CB filler particles.

### 2.2. Measurements

The linear viscoelastic response of both filled and unfilled SBR samples was measured on the rubber process analyzer RPA 2000 produced by Alpha Technologies Co. (UK).<sup>[52]</sup> This RPA can be used to measure the dynamic properties of uncured rubber as well as rubber during cure and post-cure, and it is viewed as a world standard by many industrial and research organizations.<sup>[52]</sup> A smaller sample of mass 5 g was cut from each prepared mixture. This sample was then contained within a die configuration consisting of two conical dies. Both dies can be heated using a direct contact foil heater, covering temperatures from room temperature to 503 K, with a resolution of  $\pm 0.3 \text{ K}$ . In this study, the temperature in all measurements was maintained at  $373 \pm 0.3 \text{ K}$ , which is representative of the processing temperatures for these materials in manufacturing. The RPA applies strain to a sample by oscillating the lower die at frequencies in the range 0.03–32 Hz (angular frequencies in the range  $0.2 \text{–}200 \text{ rad s}^{-1}$ ) at a strain of  $\approx 1\%$ . Torque transmitted from the lower die through the sample was measured by a torque transducer in the fixed upper die. In this study, interest was principally taken in the storage  $G'(\omega)$  and loss  $G''(\omega)$  moduli as functions of the angular frequency  $\omega$ , or the related stress relaxation function  $G(t)$  as a function of time  $t$  (see the Appendix) for both filled and unfilled SBR samples. The measured torque values were converted into these moduli by the RPA’s internal computer system. Typical results for the unfilled sample and two filled samples are presented in **Figure 1**, where both moduli are seen to follow an  $\approx \omega^{0.3}$  power law over the range from 1 to 200  $\text{rad s}^{-1}$  (**Figure 1 a,b**). With increasing filler fraction, the moduli are seen to rise and the gap between the moduli widens, while the power law exponent decreases to  $\omega^{0.15}$  (**Figure 1 c**).

## 3. The RaPiD Algorithm

In the RaPiD model,<sup>[47–50,53–55]</sup> polymers are highly coarse grained to spherical point particles. The coordinates of the particles represent the center of mass positions of the polymers. Accounting

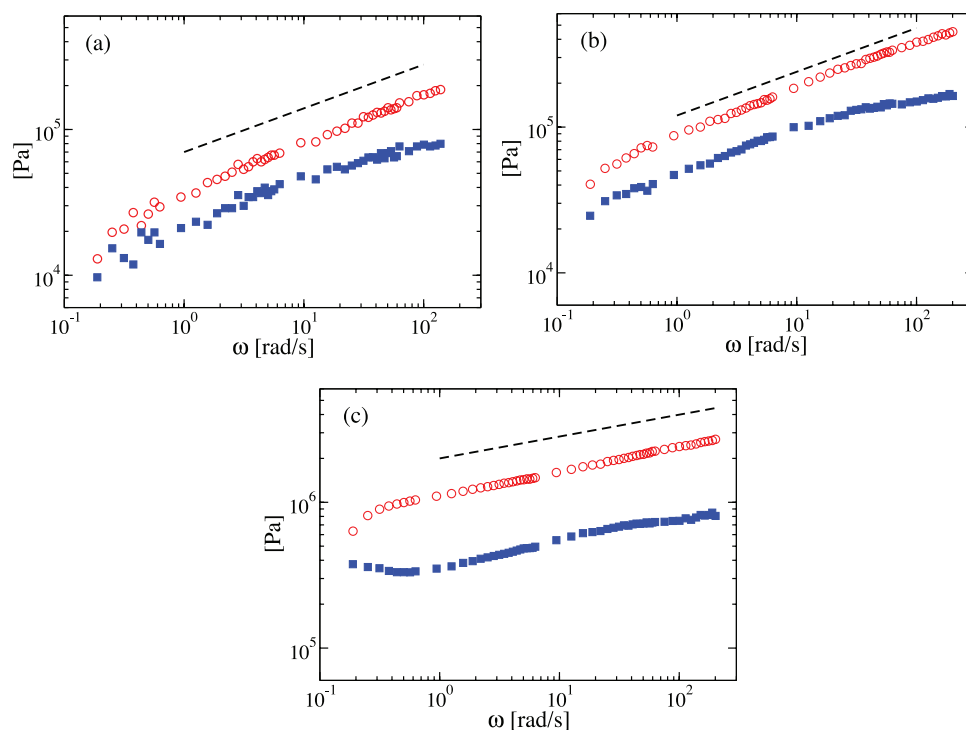


**Figure 1.** Frequency sweep measurement using a rubber process analyzer of the storage  $G'(\omega)$  (open red circles) and loss  $G''(\omega)$  (filled blue squares) moduli for a) an unfilled SBR polymer melt and for identical melts with b) 20 phr, and c) 100 phr N660 Carbon Black. Each curve represents an average over three samples. The dashed lines are  $\omega^\gamma$  power laws, where  $\gamma$  is the exponent and in (a) and (b)  $\gamma = 0.3$  while in (c)  $\gamma = 0.15$ . The variances in the measurements over the three samples in all cases are up to 10% for all frequencies. Error bars are not included given that the markers are larger than the variances.

for the slowest eliminated internal coordinates of the polymers, i.e., the entanglement effects, is crucial to obtain the correct bulk rheological properties. As described in more detail below, this is realized by introducing auxiliary dynamical coordinates whose deviations from their equilibrium values creates a transient viscoelastic response. RaPiD has been successfully applied for the simulation of shear banding effects,<sup>[50]</sup> particle alignment in sheared viscoelastic fluids,<sup>[56,57]</sup> entangled polymer melts,<sup>[58]</sup> nonlinear flow rheology in polymer solutions<sup>[49]</sup> and star polymer melts,<sup>[47]</sup> flow of polymer solutions near solid interfaces<sup>[55]</sup> and anomalous polymer chain diffusion.<sup>[59]</sup> Since RaPiD is new to the rubber field, we present a brief overview of the RaPiD algorithm; the reader is referred to earlier work for further details.

### 3.1. Potential of Mean Force

Flory–Huggins theory<sup>[60–62]</sup> was originally developed for polymer–solvent lattice models. In this study it is used—off lattice and in the absence of solvent—as an effective density-dependent potential with an asymmetric response to fluctuations around the average. Its lattice gas analogue reproduces the equation of states of many molecular liquids reasonably well.<sup>[63,64]</sup> In RaPiD, the local polymer volume fraction  $\phi_i$  near the center of the  $i^{\text{th}}$  polymer is calculated using

$$\phi_i = \frac{1}{\rho_{\max}} \sum_{j=1}^{N_p} w(r_{ij}) \quad (1)$$

where  $\rho_{\max}$  is the maximal polymer melt density, the sum runs over all  $N_p$  polymers in the system including polymer  $i$ ,  $r_{ij}$  denotes the distance between two polymer centers, and  $w(r_{ij})$  is an appropriately normalized weight function describing the density distribution associated with a polymer. As it is difficult to derive a precise function for  $w(r_{ij})$ , we selected a monotonically decaying function smoothly approaching zero at the cut-off distance  $r_c = 2.5R_g$ . Details of this function are provided in ref. [56]. The total free energy of the system is calculated by inserting the local densities in the theoretical expression from Flory–Huggins

$$\begin{aligned} \Phi_{\text{FH}}(r) &= \sum_{i=1}^{N_p} a_p(\phi_i) \\ &= pk_B T \sum_{i=1}^{N_p} \left[ \frac{1-\phi_i}{\phi_i} \ln(1-\phi_i) - \chi \phi_i \right] \end{aligned} \quad (2)$$

where  $p$  represents the number of Kuhn segments per polymer,  $k_B$  is Boltzmann's constant,  $T$  the temperature, and the Flory–Huggins parameter  $\chi$  determines the fluctuations in the density inhomogeneity. Note that the above expression excludes the translational entropy of the polymers, as these are already accounted for by the simulated particles. A full derivation of this expression, starting from Flory–Huggins theory, is provided in the Appendix of ref. [56]. The above equations define the thermodynamic behavior of the simulated polymer melt.

### 3.2. Transient Forces

Central to RaPiD is the description of the viscoelastic response that arises in any polymer system when disturbed from equilibrium. In an equilibrium melt, adjacent polymers will impose topological constraints on each other. These can be referred to as entanglements, and develop since polymers cannot cross each other. Clearly, these entanglements are lost when a coarse-grained model describes a polymeric system in terms of the polymers' centers of mass coordinates only. In RaPiD, the number of entanglements between any pair of adjacent polymers  $i$  and  $j$  is qualitatively accounted for by introducing the dynamical scalar variable  $n_{ij}$ . The reader is referred to a recent publication on extending this description to vectors.<sup>[54,65]</sup> The average number of entanglements between two polymers, in a melt in equilibrium, varies with the distance and is denoted by  $n_0(r_{ij})$ . We assume that SBR polymers are well approximated as Gaussian chains, and hence that the monomers are Gaussian distributed around the center of mass of a polymer. The overlap of the monomer distributions of two polymers is then approximately a Gaussian in the distance  $r_{ij}$  between the two chains.<sup>[66]</sup> To avoid vanishing derivatives for short distances, we use the quadratically decaying approximation

$$n_0(r_{ij}) = \begin{cases} (1 - r_{ij}/r_c)^2 & \text{for } r_{ij} \leq r_c \\ 0 & \text{for } r_{ij} > r_c \end{cases} \quad (3)$$

For two polymers in an equilibrium melt, their average number of entanglements as a function of the distance recovers  $\langle n_{ij}(r_{ij}) \rangle = n_0(r_{ij})$ . Nonequilibrium conditions and thermal fluctuations will cause  $n_{ij}$  to deviate from  $n_0(r_{ij})$  and thereby induces forces on the system. We define the "transient" potential

$$\Phi_t = \frac{1}{2} \alpha \sum_{i < j} [n_{ij} - n_0(r_{ij})]^2$$

with the positive  $\alpha$  denoting the strength, to derive the forces acting on the particles and on their number of entanglements. This quadratic function was introduced by van den Noort et al.<sup>[50]</sup> and represents the tendency of the system to relax to equilibrium by simultaneously adjusting the polymer positions and their number of entanglements. The relative relaxation rates of these two processes, to be discussed in the next section, determines which process dominates. The additional potential, with contributions for every particle pair with  $r_{ij} \leq r_c$ , does not alter the thermodynamic behavior set by the Flory–Huggins potential.

### 3.3. Propagator

Configurations are propagated in time by a Brownian dynamics scheme, subject to the two potentials discussed above.<sup>[50]</sup> The displacement of particle  $i$  over a time step  $dt$  reads as

$$d\mathbf{r}_i = -\frac{1}{\xi_i} \frac{\partial(\Phi_{FH} + \Phi_t)}{\partial \mathbf{r}_i} dt + k_B T \frac{\partial \xi_i^{-1}}{\partial \mathbf{r}_i} dt + \Theta_i \sqrt{\frac{2k_B T dt}{\xi_i}} \quad (5)$$

The first term on the righthand side represents (minus) the total potential force on the particle, and translates into a drift velocity upon division by the particle-dependent friction coefficient. The latter varies with the particle's entanglements via

$$\xi_i = \xi_e \sum_j \sqrt{|n_{ij}| n_0(r_{ij})} \quad (6)$$

where  $\xi_e$  represents the friction per entanglement. The second term in the equation of motion accounts for the position-dependence of this friction coefficient in the Itô representation, i.e., all terms are evaluated at the same time  $t$ , followed here. The final term in Equation (5) represents the erratic Brownian motion of the particle, where  $\Theta_i$  is a time-dependent Markovian random vector composed of three independent components with unit variance, zero mean and without correlations across particles. The strength of these stochastic contributions is related to the friction and temperature by the fluctuation–dissipation theorem, which is included in the last term.

The evolution of the number of entanglements  $n_{ij}$  follows the expression

$$dn_{ij} = -\frac{1}{\alpha \tau} \frac{\partial \Phi_t}{\partial n_{ij}} dt + \Theta_{ij} \sqrt{\frac{2k_B T dt}{\alpha \tau}} \quad (7)$$

where the first term on the righthand side results in the exponential relaxation of  $n_{ij}$  to  $n_0(r_{ij})$  with a characteristic relaxation time  $\tau$ , while the second term describes Brownian fluctuations. The time-dependent Markovian random numbers  $\Theta_{ij}$  have zero mean, unit variance, and are uncorrelated across particle pairs. Again, a fluctuation–dissipation theorem couples the strength of the stochastic term to the friction ( $\alpha \tau$ ) in the first term. Since polymers in close proximity to each other tend to be more interwoven, and consequently relax their entanglements slower than the less entangled polymers at larger separations, the relaxation time is expressed as

$$\tau(r_{ij}) = \tau_0 \exp\left(-\frac{r_{ij}}{\lambda}\right) \quad (8)$$

with  $\tau_0$  the relaxation time at zero distance and  $\lambda$  the decay distance of the relaxation time.

### 3.4. Filler Particles

For this study, the carbon black filler particles are approximated as spherical colloids. To keep the computational demands manageable, the radius of these particles was taken as  $R_f = 2R_g = 20$  nm, about two-thirds of the radius of the primary carbon black particles. Two particles  $i$  and  $j$  interact by a purely repulsive potential

$$\phi_{ff}(r_{ij}) = \epsilon_{ff} \left( \frac{a_{ff}}{d_{ij}} \right)^8 \quad (9)$$

based on the nearest distance between their surfaces,  $d_{ij} = r_{ij} - 2R_f$ . The strength and length scale are set as  $\epsilon_{ff} = 4k_B T$  and  $a_{ff} = 0.1R_g$ , respectively. The filler particles are propagated by conventional Brownian dynamics, with a friction constant  $\xi_f = 7 \times 10^{-7}$  kg s<sup>-1</sup>,

**Table 1.** Summary of the properties of the styrene–butadiene rubber (SBR), the N660 Carbon Black filler particles, and the parameters entering the simulation. The experimental linear rheology of the unfilled SBR is reproduced in the simulations by tuning the bulk parameters  $\alpha$ ,  $\xi_e$ ,  $\tau_0$ , and  $\lambda$ .

Description	Symbol	Value	Unit
<b>Polymer characteristics</b>			
Molecular weight	$M_w$	370	kg mol <sup>-1</sup>
Polydispersity index		2.1	–
Radius of gyration <sup>a)</sup>		10, 20, 40	nm
Radius of gyration in simulations	$R_g$	10	nm
Kuhn segments per polymer	$p$	3000	–
<b>Bulk parameters</b>			
Flory–Huggins parameter	$\chi$	0.5	–
Entanglement fluctuations	$\alpha$	15	$k_B T$
Entanglement friction	$\xi_e$	$1 \times 10^{-6}$	kg s <sup>-1</sup>
Maximum relaxation time	$\tau_0$	5	s
Decay length of relaxation time	$\lambda$	0.5	$R_g$
Mass density of polymer melt	$\rho_{\max}$	900	kg m <sup>-3</sup>
Glass transition temperature	$T_g$	253	K
<b>Experimental conditions</b>			
Temperature	$T$	373	K
<b>Filler particles (CB N660)</b>			
Average particle radius <sup>b)</sup>		$31.5 \pm 18$	nm
Particle radius in simulations	$R_f$	20	nm

<sup>a)</sup>Measured in THF solution using GPC.; <sup>b)</sup>CORAX technical datasheet.

a value previously used in simulations of colloids in a wormlike micellar solution.<sup>[56]</sup> This value is also comparable to the SBR entanglement friction given in **Table 1**. In simulations with inert filler particles, their interaction with the polymers is described by a potential based on the sphere-polymer distribution function<sup>[67]</sup>

$$\Phi_{\text{pf}}^{\text{rep}}(r_{ij}) = \epsilon_{\text{pf}}^{\text{rep}} \exp \left[ -\frac{(r_{ij} + R_g - R_f)^2}{2b_{\text{pf}}^2} \right] \quad (10)$$

with strength  $\epsilon_{\text{pf}}^{\text{rep}} = 100k_B T$  and decay distance  $b_{\text{pf}} = \frac{1}{2}R_g$ . The conformational flexibility of the polymer makes this potential very soft; a polymer's center of mass may even reside within a filler's excluded volume—while the polymer's atoms clearly may not—for a polymer wrapped around a filler particle. Reversible attachment of polymers at the fillers surface is modeled by a standard Lennard-Jones potential

$$\Phi_{\text{pf}}^{\text{LJ}}(r_{ij}) = 4 \epsilon_{\text{pf}}^{\text{LJ}} \left[ \left( \frac{\sigma_{\text{pf}}}{r_{ij}} \right)^{12} - \left( \frac{\sigma_{\text{pf}}}{r_{ij}} \right)^6 \right] \quad (11)$$

with strength  $\epsilon_{\text{pf}}^{\text{LJ}}$  and radius  $\sigma_{\text{pf}} = R_f = 2R_g$ . Since the bound rubber layer surrounding a filler particle typically measures

around 10 nm in thickness,<sup>[1,9,28–30,35]</sup> the potential is smoothly truncated at a distance of  $R_f + 10 \text{ nm} = 3R_g$ . This approach does not account for individual monomers of a particular polymer being closer to the filler than the center of mass of the polymer.

### 3.5. Simulation Set Up

The model parameters entering the simulations were, as much as possible, based on the properties of the experimental samples. An overview of these parameters is provided in **Table 1**. For convenience, the polymers are assumed monodisperse. The monomer density in a melt will be close to  $\rho_{\max}$ , resulting in local volume fractions  $\phi_i$  close to unity. Since this leads to the divergence of the Flory–Huggins free-energy, see Equation (2), we use the expedient of reducing the average mass density to  $\rho_p = 0.9\rho_{\max}$ . A satisfying homogeneous melt was obtained by selecting  $\chi = 0.5$ . The simulation parameters relating to the entanglements are less straightforwardly related to the polymer characteristics. Instead, the values of  $\alpha$ ,  $\xi_e$ ,  $\tau_0$ , and  $\lambda$  are obtained by tuning the stress relaxation modulus of the simulated melt to the experimental counterpart, as discussed in the results section.

All simulations were performed using cubic boxes subject to periodic boundary conditions. For the unfilled melt, the system was initialized by randomly distributing 1500 polymer particles in a box with sides of  $L = 8R_g$ . Filled systems were initiated by randomly placing  $N_f = 40$  spherical filler particles in the box, subject to excluded volume constraints. Boxes with a filler content of  $x$  phr have edges of length

$$L = 4R_g \left[ \frac{\pi}{6} N_f \left( 1 + \frac{100\rho_f}{x\rho_p} \right) \right]^{\frac{1}{3}} \quad (12)$$

Polymer particles are placed randomly, at a density  $\rho_p$ , throughout the volume not already occupied by the filler particles. With  $x$  varying from 20 to 100, box sizes range from  $\approx 16$  to  $\approx 25R_g$  and the number of polymers varies from 8805 to 44028.

## 4. Results

### 4.1. Rheology of Unfilled SBR

The experimental storage and loss moduli of the unfilled SBR sample are presented in **Figure 1 a**. The corresponding stress relaxation function, requiring four Maxwell modes (see Appendix) for a good fit over the frequency range, is shown in **Figure 2**, with the coefficients of  $G_4^{\text{exp}}(t)$  summarized in **Table 2**. The fit reveals that the relaxation time of the fourth mode is considerably longer than that of the three other modes, and thereby presents a severe challenge to the simulations. Rather than being diverted by the very long simulations required to establish simulation parameters that reproduce this wide range of time scales, we suppress the fourth mode to gain access to our research question, the impact of filler particles on the melt rheology in RaPiD. To retain the plateau

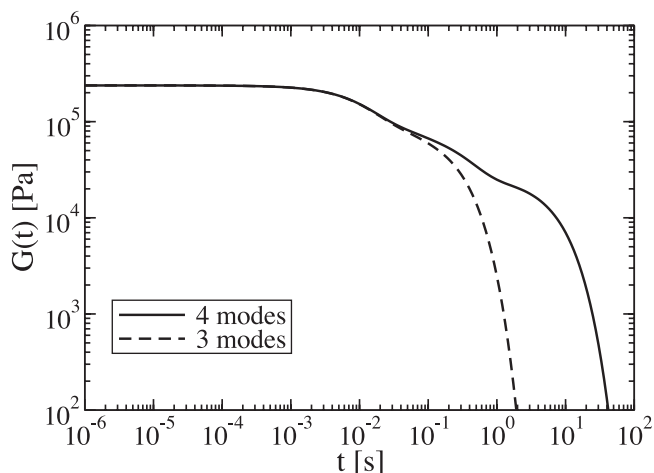


**Figure 2.** The stress relaxation moduli  $G_4^{\text{exp}}(t)$  of the unfilled sample (solid line), obtained by fitting the experimental data in Figure 1 with four Maxwell modes. The slowest mode has been removed in  $G_3^{\text{exp}}(t)$  (dashed line), while increasing the weight of the slowest-but-one mode, see Table 2. The fluctuations in the curves result from the limited number of Maxwell modes in the fits.

value of  $G_4^{\text{exp}}(t)$  at low times, we construct  $G_3^{\text{exp}}(t)$  by copying the parameters of the first three modes and adding the amplitude of the fourth mode to the amplitude of the third mode (see Table 2). Plots of the resulting stress relaxation modulus and of the storage and loss moduli are presented in Figure 2 and Figure 3, respectively. In the time domain, it is clear that the short-time response has been conserved while the slow decay beyond 0.1 s scale has been curtailed. In the frequency domain, the four-mode fit closely follows the experimental data over the entire frequency domain of the measurements. With the exclusion of the fourth mode, the crossover frequency shifts from  $\omega \approx 10^{-2} \text{ rad s}^{-1}$  (outside the experimental range) to  $\omega \approx 3 \text{ rad s}^{-1}$ . More importantly, the three-mode Maxwell model gives a reasonable description of the experimental storage and loss moduli for  $3 \leq \omega \leq 10^2 \text{ rad s}^{-1}$ , with the most pronounced deviation at the low frequency end. We will therefore focus on this frequency range in simulations and experiments of unfilled and filled SBRs.

The dynamics-related parameters of the RaPiD model are obtained by trial-and-error optimization of the agreement between the simulated stress relaxation function  $G^{\text{sim}}(t)$  and the three-mode experimental curve  $G_3^{\text{exp}}(t)$ . To outline the

**Table 2.** Coefficients obtained by fitting the experimental storage and loss moduli of the unfilled SBR melt with a four mode Maxwell model (see Equations (A.5) and (A.6)) and their reduction to a three mode model.

$i$	$n = 4$		$n = 3$	
	$G_i$ [Pa]	$\tau_i$ [s]	$G_i$ [Pa]	$\tau_i$ [s]
1	125.3	0.011	125.3	0.011
2	31.9	0.038	31.9	0.038
3	54.3	0.287	80.9	0.287
4	26.6	7.511		

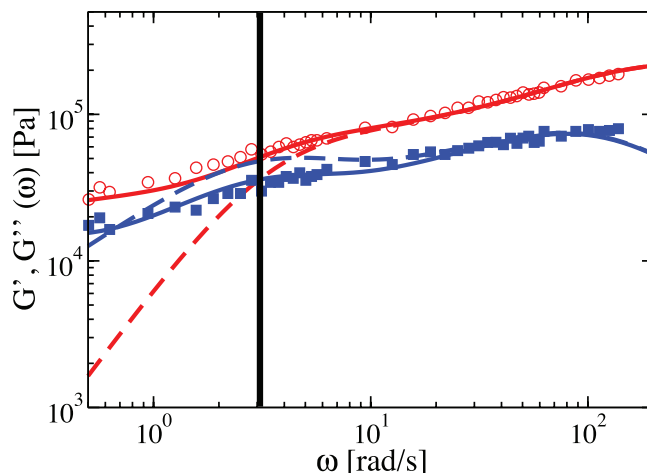


**Figure 3.** The storage (red) and loss (blue) moduli calculated from the four-mode  $G_4^{\text{exp}}(t)$  (solid lines) and three-mode  $G_3^{\text{exp}}(t)$  (dashed lines) fits to the experimental data (markers) for the unfilled SBR melt. The solid black line is approximately the lowest frequency of relevance in this study.

optimization process we summarize here the findings of an extensive parameter study with RaPiD.<sup>[49]</sup> First, the initial plateau value of  $G^{\text{sim}}(t)$  increases with the strength  $\alpha$  of the transient forces. Second, slowing of the dynamics can be achieved by increasing the time constant  $\tau_0$  and/or the friction coefficient  $\xi_e$ , thus shifting the curve to longer timescales. Finally, the transition from plateau to the tail becomes smoother with the introduction of more relaxation times by decreasing the relaxation distance  $\lambda$ .

The best fit for the data set from Figure 1 a is presented in Figures 4 and 5 in the time and frequency domain, respectively with the parameter values given in Table 1. Good correspondence is achieved between the simulated stress relaxation function and the target function  $G_3^{\text{exp}}(t)$ , while a satisfactory agreement is obtained for the storage and loss moduli for  $\omega > 3 \text{ rad s}^{-1}$ . First, the strengths of the dominant mechanisms,

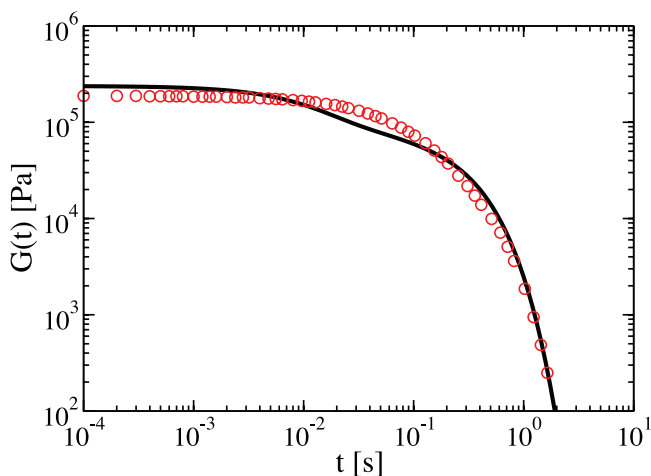


**Figure 4.** Stress relaxation moduli for the unfilled SBR melt in the RaPiD simulations,  $G^{\text{sim}}(t)$  (open red circles), and the target  $G_3^{\text{exp}}(t)$  extracted from the experiments (solid line). The slight step in  $G_3^{\text{exp}}(t)$  around  $5 \times 10^{-2} \text{ s}$  is an artefact reflecting the low number of Maxwell modes, and therefore was ignored when tuning the simulation model.

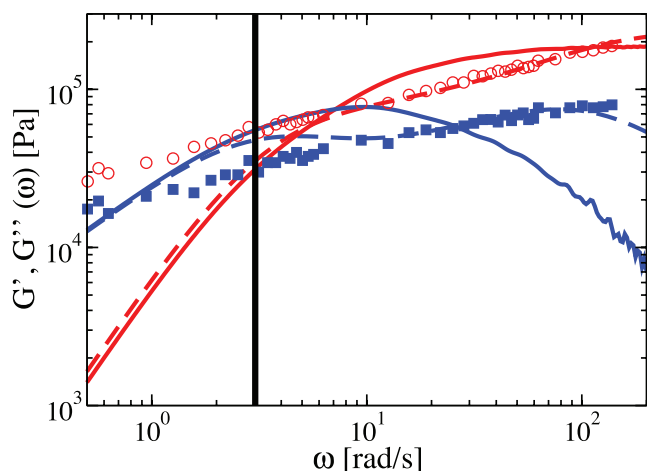


**Figure 5.** The storage (red) and loss (blue) moduli of the unfilled SBR melt as obtained by experiments (markers), the three-mode approximation  $G_3^{\text{exp}}$  (dashed lines) and the RaPiD simulations (solid lines). The solid black line is approximately the lowest frequency of relevance in this study.

i.e., viscous response below the crossover frequency and elastic response above this frequency, are well described by the simulation model. Second, the crossover frequency for the simulation trends is slightly higher than for  $G_3^{\text{exp}}$ . Third, the low frequency range of  $G_3^{\text{exp}}$  is well-fitted. Only for the loss modulus at high frequencies do we observe an appreciable deviation, approaching an order of magnitude at the end of the experimental frequency range. We do not expect to recover agreement at this large frequency range, i.e.,  $\omega > 100 \text{ rad s}^{-1}$ , as RaPiD is unable to resolve this range due to the coarse-graining of all degrees of freedom associated with a high frequency response. This behavior has been observed in previous studies with RaPiD.<sup>[47,49]</sup> In conclusion, the model provides an adequate description of the linear rheological response of an unfilled SBR melt over the time and frequency ranges of interest in this study.

#### 4.2. Rheology of Filled SBR

We now turn our attention to the impact of filler particles on the rheological properties of the SBR melt. We highlight that for simplicity the filler particles are represented as individual spherical particles rather than nonspherical aggregates as in the experimental samples, as we are principally interested in a qualitative description of the rheological properties. Experimental data on two filled samples are provided in Figure 1 b,c. These figures clearly show that the inclusion of filler particles and the introduction of interfacial bound rubber layers, both with their own rheological properties, affect the overall viscoelastic response of the samples. The generalized Maxwell model is again applied to convert the moduli into a stress relaxation function, this time requiring five modes for an adequate description over the entire frequency range. Akin to the situation for the unfilled sample, the last mode is considerably slower than the preceding modes. Since we are mainly interested in the angular frequency range accessible by simulations, from 1 to  $100 \text{ rad s}^{-1}$ , we once more eliminate the last mode after adding

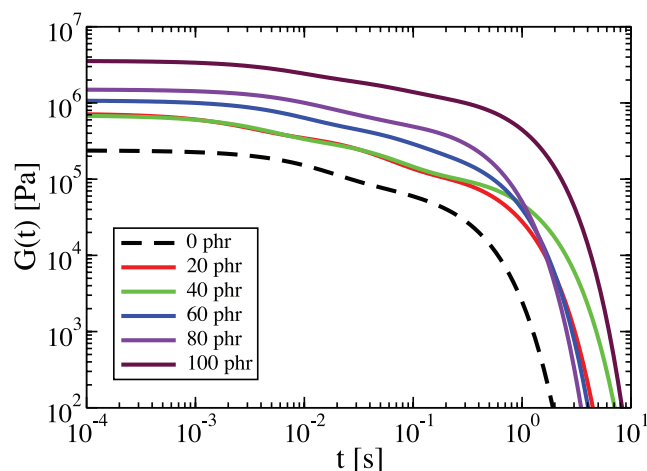


**Figure 6.** Stress-relaxation functions  $G_4^{\text{exp}}(t)$  constructed by fitting the experimental data with a generalized Maxwell model, for SBR melts containing 20–100 phr N660 Carbon Black (see legend). The relaxation function  $G_3^{\text{exp}}(t)$  of the unfilled melt (0 phr) is included for comparison purposes (dashed line).

its weight to that of the penultimate mode to retain the short-time plateau in  $G(t)$ . The four-mode stress relaxation functions  $G_4^{\text{exp}}(t)$  extracted from the experiments on the filled samples are collected in **Figure 6**. With increasing filler fraction, the short-time plateau steadily increases in height and lasts for longer times. The rise of the plateau value with filler concentration is monotonic, though the samples with 20 and 40 phr are remarkably similar up to the 0.1 s time scale, while the onset of the decaying tail is less regular. The changes in the moduli are in part due to the rigid filler particles and in part due to the interaction between fillers and polymers. In exploring whether these effects can be described qualitatively and quantitatively by the RaPiD model, it is assumed that the parameters of the melt remain unchanged. We impose the restriction that the freedom in optimizing the agreement between experiments and simulations is limited to the polymer–filler interaction from now on.

The simulated stress relaxation functions of filled melts with the filler particles interacting by excluded volume interactions only, see Equations (9) and (10), are presented in **Figure 7**. With increasing filler concentration the initial plateau rises and the onset of the tail is delayed, but the shifts are less pronounced than for the experimental samples. The nonmonotonic increment of the plateau value probably reflects the limited length of the simulations. The inclusion of polymer–filler binding appears to be imperative to recover quantitative agreement with the experimental data.

The effect of an attractive CB–SBR interaction on the stress-relaxation functions of the filled SBR compounds is shown in **Figure 8**. By varying  $\epsilon_{\text{pf}}^{\text{lj}}$  we explored its effect on  $G^{\text{sim}}(t)$  for all filler concentrations. Interestingly, a small interaction strength of  $\epsilon_{\text{pf}}^{\text{lj}} = 0.1k_{\text{B}}T$  suffices to quantitatively recover the experimental material reinforcement with increasing filler concentration, see **Figure 6**, unlike the modest increase obtained with purely repulsive CB–SBR interaction. To highlight this effect, the plateau values of  $G(t)$  at  $t = 10^{-3} \text{ s}$  for the experimental and simulated systems are collected in **Figure 9**. The system with a weakly attractive CB–SBR interaction qualitatively reproduces

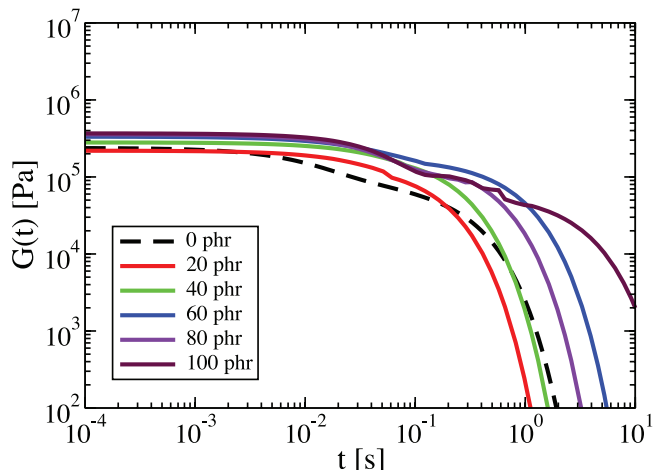


**Figure 7.** Stress relaxation functions  $G(t)$  in RaPiD simulations for SBR melts containing inert spherical filler particles at concentrations from 20 to 100 phr (see legend). The relaxation function  $G_3^{\text{exp}}(t)$  of the unfilled melt (0 phr) is included for comparison purposes (dashed line).

the trend of increasing the plateau by over an order of magnitude with the inclusion of 100 phr filler particles, even obtaining near quantitative agreement at both 20 and 100 phr, while the system with a purely repulsive CB–SBR interaction shows in a substantially smaller increment of the plateau. Comparing the experimental stress-relaxation functions of Figure 6 with their simulation counterparts in Figures 7 and 8, one notices that the onset of the exponential tail becomes modestly delayed with increasing filler fraction in the experimental systems, the delay has largely vanished in the simulated systems with excluded volume interactions, while the simulated systems with weak attractions show an earlier onset of the exponential decay. The earlier onset of the exponential decay in Figure 8 in comparison to the case with a repulsive polymer-filler interaction (Figure 7) may be due to a number of factors such as the nature of the

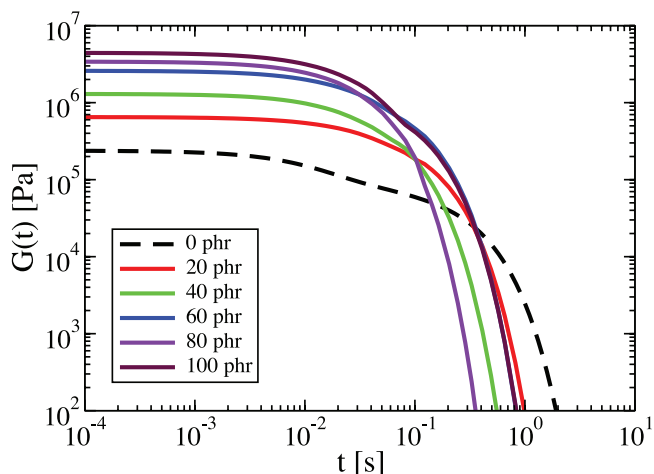


**Figure 8.** Stress relaxation functions  $G(t)$  in RaPiD simulations for SBR melts containing noninert spherical filler particles, at concentrations from 20 to 100 phr (see legend), for a filler–polymer binding strength  $\epsilon_{\text{pf}}^{\text{LJ}} = 0.1k_{\text{B}}T$ . The relaxation function  $G_3^{\text{exp}}(t)$  of the unfilled melt (0 phr) is included for comparison purposes (dashed line).

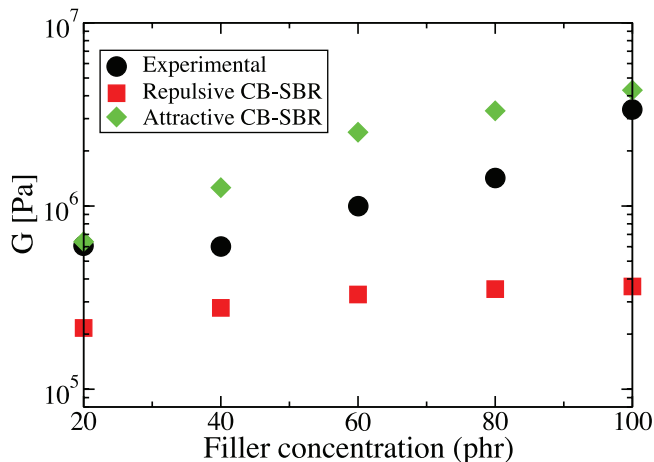


**Figure 9.** Comparison of the magnitudes of the plateau values of  $G(t)$  at  $t = 10^{-3}$  s from experiments (Figure 6), from simulations with purely repulsive CB–SBR interactions (Figure 7) and from simulations with weakly attractive CB–SBR attractions (Figure 8,  $\epsilon_{\text{pf}}^{\text{LJ}} = 0.1k_{\text{B}}T$ ).

polymer–filler attraction. Further exploration of this interaction potential and also the filler geometry in future simulations would prove useful towards understanding this response.

The storage and loss moduli for the 100 phr compounds with weakly attractive CB–SBR interactions have been calculated from  $G^{\text{sim}}(t)$  using Equations (A.3) and (A.4). The results are presented in Figure 10, along with the experimental storage and loss moduli at 100 phr and the moduli extracted from  $G_4^{\text{exp}}(t)$ . Recall that the low-frequency terminal region to  $G_4^{\text{exp}}(t)$  is artificial as we have excluded the slowest relaxation mode from the generalized Maxwell fit to the experimental data, and a similar procedure was applied to obtain the target stress-relaxation function at 0 phr to which the simulation parameters of the melt were tuned. Given these conditions, the agreement

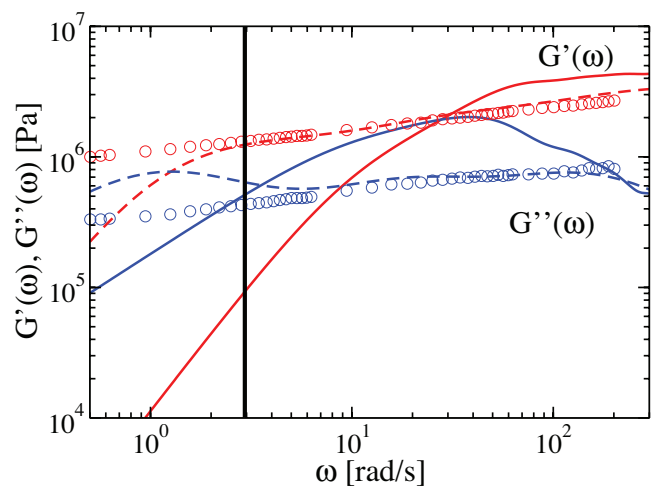


**Figure 10.** Comparison of the storage (in red) and loss (in blue) moduli from experiments (open circles), Fourier transform using Equation (A.3) and Equation (A.4) of  $G_4^{\text{exp}}(t)$  (dashed lines) and from RaPiD simulations (solid lines) for 100 phr. The CB–SBR interaction is the attractive Lennard-Jones potential given by Equation (11). The solid black line is approximately the lowest frequency of relevance in this study.

in Figure 10 is reasonable, with the simulated moduli being of the same order as the experimental moduli over nearly two decades in frequency space, although it is also evident that the model does not capture the approximately power-law behavior of the experimental data. The best qualitative agreement is observed for  $G'(\omega)$  where simulations replicate the experimental data well within an order of magnitude for  $\omega > 6 \text{ rad s}^{-1}$ . The simulations overestimate  $G''(\omega)$  over the frequency range up to the maximum frequency accessible to experiments  $\omega \approx 200 \text{ rad s}^{-1}$ . However, it does so by less than an order of magnitude in this frequency regime. Quantitative differences between the simulations and experiments, particularly in relation to the crossover of  $G'$  and  $G''$  in Figure 10, can in part be attributed to differences in the description of the filler particles. The accurate inclusion of filler aggregates, such as those found in the laboratory experimental samples, may also require changes to the filler–polymer interaction. A description of filler aggregates is outside the scope of this preliminary study but will be considered in the next model iteration.

## 5. Discussion and Conclusion

In this proof-of-concept study, RaPiD was applied for the first time to SBR melts and SBR-melts filled with CB. In RaPiD, an entire polymer is modeled as a single anisotropic particle interacting with its neighbors by a conservative potential as well as by transient forces qualitatively accounting for entanglement effects; the fillers are represented here as spherical inclusions. The standard potentials used here could be tuned to yield satisfactorily qualitative agreement with experimental data on the pure melt, suggesting that further improvements can be achieved by continued development of these potentials. Upon inserting filler particles in the simulations, only the polymer–filler interactions were tuned to obtain qualitative agreement with experimental data on filled melts.

Of general interest is the interaction between the filler particles and the polymers. The simulations indicate that merely accounting for the excluded volume interactions does not suffice to explain the increase of the plateau value of the stress relaxation function with increasing filler fraction. Instead, an attraction between fillers and polymers is required. The optimum interaction strength established in this study,  $\epsilon_{\text{pt}}^{\text{I}} = 0.1 k_{\text{B}}T$ , indicates that this strength is not related to the polymer–filler binding interaction, which clearly is much stronger. We surmise that this low value reflects the effective strength of the interaction between two filler particles generated by the intermediate polymers. At the atomistic level the attraction results from polymer bridges connecting two filler particles acting as entropic-springs between the filler particles, whereas in the highly coarse-grained simulations this effect is mimicked by polymer particles positioned between two filler particles exerting weak attractive forces on both filler particles.

Having established that RaPiD can qualitatively capture the main features of an SBR melt and CB-filled SBR melts, the challenge for future work is to improve the model to obtain a more quantitative agreement with predictive potential. This model could be used to study the distribution of filler clusters, to investigate the effect of differing filler types and

geometries on the material strengthening and to explore the emergence of the Payne and Mullins effects in crosslinked filled elastomers. Investigation of the Payne and Mullins effects will require the inclusion of irreversible breaking interactions. We could also use the model to calculate estimates of the confidence intervals for the RaPiD parameters in a similar manner to our previous study.<sup>[49]</sup> In addition, the nonlinear rheological response of the crosslinked filled elastomers will be explored. Earlier simulations with the RaPiD model indicated that the conservative potential affects the storage and loss moduli at high frequencies, hence further developments in that area are needed to improve agreement with experiments on melts for high frequencies. At low frequencies, the procedure to remove the slowest mode must be reconsidered and the frequency range of the model should be extended to include more slow modes. The filler particles in the simulations were simple spherical particles, whereas carbon black used in SBR melts consists of fractal aggregates of near-spherical primary particles. These complex shapes are likely to affect their ability to bind polymers, contributing to the so-called occluded rubber, and will alter the steric interactions between the aggregates. Using a recently developed algorithm for the translational and rotational Brownian dynamics of arbitrarily shaped rigid clusters,<sup>[68]</sup> it is becoming possible to explore the impact of (distribution of) filler clusters on the rheology of melts. The effect of variable filler particle geometry and size on the material strengthening will be explored in a future investigation. This is currently a highly debated topic in the field of filled elastomers.<sup>[69–72]</sup> However, additional developments of the model will be necessary to include the presence of permanent crosslinks in rubber.

## Appendix: Moduli

In RaPiD simulations, the stress tensor at time  $t$  is calculated as

$$\sigma_{\alpha\beta}(t) = -\frac{1}{V} \sum_{i < j} r_{ij,\alpha} F_{ij,\beta} \quad (\text{A.1})$$

where  $V$  denotes the volume of the system, the sum runs over all particle pairs,  $r_{ij,\alpha}$  denotes the  $\alpha$  component of the vector connecting two particles  $i$  and  $j$ , and  $F_{ij,\beta}$  is the  $\beta$  component of the conservative forces between these two particles. The stress relaxation modulus is obtained as the autocorrelation of the off-diagonal elements of the stress tensor

$$G^{\text{sim}}(t) = \frac{V}{k_{\text{B}}T} \langle \sigma_{xy}(\tau) \sigma_{xy}(\tau + t) \rangle \quad (\text{A.2})$$

where the average is over the time  $\tau$ . The storage and loss moduli, as measured by the RPA, then follow from

$$G'(\omega) = \omega \int_0^{\infty} \sin(\omega t) G(t) dt \quad (\text{A.3})$$

$$G''(\omega) = \omega \int_0^{\infty} \cos(\omega t) G(t) dt \quad (\text{A.4})$$

In practice, this requires the judicious fitting of the slowly decaying noisy tail to  $G^{\text{sim}}(t)$  with a decaying exponential, followed by combined numerical and analytical evaluation of the integrals. The alternative sees the measurement data converted from the frequency domain to the time domain by fitting the data over the available frequency range with an  $n$  mode generalized Maxwell model,

$$G'(\omega) = \sum_{i=1}^n G_i \frac{\tau_i^2 \omega^2}{1 + \tau_i^2 \omega^2} \quad (\text{A.5})$$

$$G''(\omega) = \sum_{i=1}^n G_i \frac{\tau_i \omega}{1 + \tau_i^2 \omega^2} \quad (\text{A.6})$$

where  $G_i$  and  $\tau_i$  are the strength and characteristic time of the  $i^{\text{th}}$  Maxwell mode respectively. Using the  $2n$  parameter values obtained by a least squares fit of the logarithm of the theoretical moduli to their experimental counterparts, the stress relaxation modulus is calculated as

$$G_n^{\text{exp}}(t) = \sum_{i=1}^n G_i \exp(-t/\tau_i) \quad (\text{A.7})$$

Both conversions are used in this study.

## Acknowledgements

This project was carried out in the framework of the innovation program Gelderland & Overijssel Gebundelde Innovatiekracht and cofunded by the European Regional Development Fund. The project partners Apollo Tyres Global R&D (Enschede, The Netherlands), the Tyre-Road Consortium of the University of Twente and Elastomer Research Testing B.V. (ERT, Deventer, The Netherlands) are gratefully acknowledged for their assistance. B.W.F. acknowledges E. Cichomski and W. Dierkes of the Elastomer Technology and Engineering group, University of Twente, for assistance in preparing the samples and operating the RPA.

## Conflict of Interest

The authors declare no conflict of interest.

## Keywords

coarse grained simulations, elastomers, filled and unfilled polymers, mesoscopic model, rheology

Received: March 1, 2018

Revised: April 20, 2018

Published online: May 24, 2018

[1] B. Omnès, S. Thuillier, P. Pilvin, Y. Grohens, S. Gillet, *Composites, Part A* **2008**, 39, 1141.

[2] J. L. LeBlanc, *J. Appl. Polym. Sci.* **2011**, 122, 599.

[3] J. L. LeBlanc, *J. Appl. Polym. Sci.* **1997**, 66, 2257.

[4] C. Robertson, C. Lin, M. Rackaitis, C. Roland, *Macromolecules* **2008**, 41, 2727.

- [5] A. Mongruel, M. Cartault, *J. Rheol.* **2006**, 50, 115.
- [6] J. L. LeBlanc, A. Staelraeve, *J. Appl. Polym. Sci.* **1994**, 53, 1025.
- [7] P. Berki, R. Gobl, J. Karger-Kocsis, *Polym. Test.* **2017**, 61, 404.
- [8] P. Berki, J. Karger-Kocsis, *J. Macromol. Sci., Part B* **2016**, 55, 749.
- [9] J. Berriot, H. Montés, F. Lequeux, D. Long, P. Sotta, *Macromolecules* **2002**, 35, 9756.
- [10] N. Rattanasom, T. Saowapark, C. Deerprasertkul, *Polym. Test.* **2007**, 26, 369.
- [11] N. Suzuki, Y. Kamachi, K. Takai, S. Kiba, Y. Sakka, N. Miyamoto, Y. Yamauchi, *Eur. J. Inorg. Chem.* **2014**, 17, 2773.
- [12] S. Mihara, D. N. Datta, J. W. M. Noordermeer, *Rubber Chem. Technol.* **2009**, 82, 524.
- [13] W. Kaewsakul, K. Sahakaro, W. K. Dierkes, J. W. M. Noordermeer, *Rubber Chem. Technol.* **2013**, 86, 313.
- [14] W. Kaewsakul, K. Sahakaro, W. K. Dierkes, J. W. M. Noordermeer, *Rubber Chem. Technol.* **2012**, 85, 277.
- [15] K. Sisanth, M. Thomas, J. Abraham, S. Thomas, in *Progress in Rubber Nanocomposites* (Eds: S. Thomas, H. J. Maria), Woodhead Publishing Series in Composites Science and Engineering, Woodhead Publishing, Cambridge **2017**, pp. 1–39.
- [16] W. M. Rzymiski, A. Smejda-Krzewicka, J. Rogoza, A. Ochendusko, *Influence of Selected Silica Fillers on the Properties of Vulcanised Rubber Blends*, Springer International Publishing, Cham, **2017**, pp. 517–525.
- [17] O. A. Al-Hartomy, A. A. Al-Ghamdi, S. A. F. A. Said, N. Dishovsky, M. Mihaylov, M. Ivanov, *J. Comp. Mater.* **2016**, 50, 377.
- [18] N. Rattanasom, S. Prasertsri, *Polym. Test.* **2009**, 28, 270.
- [19] R. Sengupta, M. Bhattacharya, S. Bandyopadhyay, A. K. Bhowmick, *Prog. Polym. Sci.* **2011**, 36, 638.
- [20] T.-H. Lin, Y.-S. Chien, W.-M. Chiu, *Int. J. Green Energy* **2017**, 14, 97.
- [21] M. Sienkiewicz, H. Janik, K. Borzędowska-Labuda, J. Kucińska-Lipka, *J. Cleaner Prod.* **2017**, 147, 560.
- [22] C.-H. Lai, C.-H. Lin, C.-C. Liao, *Air Qual., Atmos. Health* **2017**, 10, 1281.
- [23] A. R. Payne, *J. Appl. Polym. Sci.* **1963**, 7, 873.
- [24] L. Mullins, *Rubber Chem. Technol.* **1969**, 42, 339.
- [25] J. Diani, B. Fayolle, P. Gilormini, *Eur. Polym. J.* **2009**, 45, 601.
- [26] L. Mullins, *J. Rubber Res.* **1947**, 16, 275.
- [27] S. Cantournet, R. Desmorat, J. Besson, *Int. J. Solids Struct.* **2009**, 46, 2255.
- [28] S. Merabia, P. Sotta, D. R. Long, *Macromolecules* **2008**, 41, 8252.
- [29] D. Sodhani, S. Reese, *Macromolecules* **2014**, 47, 3161.
- [30] M. J. Wang, *Rubber Chem. Technol.* **1998**, 71, 520.
- [31] D. F. Twiss, *J. Soc. Chem. Ind.* **1925**, 44, 1067.
- [32] S.-S. Choi, *Poly. Adv. Technol.* **2000**, 55, 161.
- [33] C. M. Blow, *Polymer* **1979**, 14, 309.
- [34] D. Gabriel, A. Karbach, D. Drechsler, J. Gutmann, K. Graf, S. Kheirandish, *Colloid Polym. Sci.* **2016**, 294, 501.
- [35] J. Berriot, F. Lequeux, L. Monnerie, H. Montés, D. Long, P. Sotta, *J. Non-Cryst. Solids* **2002**, 307–310, 719.
- [36] A. Papon, T. C. L. Guy, K. Saalwächter, J. Oberdisse, S. Merabia, D. Long, P. Sotta, H. H. Frielinghaus, A. Radulescu, Demé, L. Noirez, H. Montes, F. Lequeux, *Kautsch. Gummi, Kunstst., Asbest* **2013**, 66, 52.
- [37] R. Dargazany, M. Itskov, *Phys. Rev. E* **2013**, 88, 012602.
- [38] J. S. Bergström, M. C. Boyce, *J. Mech. Phys. Solids* **1998**, 46, 931.
- [39] J. S. Bergström, M. C. Boyce, *Mech. Mater.* **2001**, 33, 523.
- [40] J. Liu, S. Wu, L. Zhang, W. Wang, D. Cao, *Phys. Chem. Chem. Phys.* **2011**, 13, 518.
- [41] C. Batistakis, M. A. J. Michels, A. V. Lyulin, *AIP Conf. Proc.* **2014**, 1599, 62.
- [42] T. V. M. Nodoro, E. Voyiatzis, A. Ghanbari, D. N. Theodorou, M. C. Böhm, F. Müller-Plathe, *Macromolecules* **2011**, 44, 2316.
- [43] D. Brown, P. Mélé, S. Marceau, N. D. Albérola, *Macromolecules* **2003**, 36, 1395.

- [44] J. Liu, Y. Gao, D. Cao, L. Zhang, Z. Guo, *Langmuir* **2011**, *27*, 7926.
- [45] D. R. Long, P. Sotta, *Macromolecules* **2006**, *39*, 6282.
- [46] D. R. Long, P. Sotta, *Rheol. Acta* **2007**, *46*, 1029.
- [47] B. W. Fitzgerald, H. Lentzakis, G. Sakellariou, D. Vlassopoulos, W. J. Briels, *J. Chem. Phys.* **2014**, *141*, 114907.
- [48] W. J. Briels, *Soft Matter* **2009**, *5*, 4401.
- [49] I. S. Santos de Oliveria, B. W. Fitzgerald, W. K. den Otter, W. J. Briels, *J. Chem. Phys.* **2014**, *140*, 104903.
- [50] A. van den Noort, W. K. den Otter, W. J. Briels, *Europhys. Lett* **2007**, *80*, 28003.
- [51] A. van den Noort, W. J. Briels, *J. Non-Newton Fluid Mech.* **2008**, *152*, 148.
- [52] J. Dick, C. Harmon, A. Vare, *Polym. Test.* **1999**, *18*, 327.
- [53] J. T. Padding, E. van Ruymbeke, D. Vlassopoulos, W. J. Briels, *Rheol. Acta* **2010**, *49*, 473.
- [54] B. W. Fitzgerald, W. J. Briels, *Macromol. Theory Simul.* **2017**, *27*, 1700069.
- [55] V. R. Ahuja, J. van der Gucht, W. J. Briels, *J. Chem. Phys.* **2016**, *145*, 194903.
- [56] I. Santos de Oliveira, A. van den Noort, J. Padding, W. K. den Otter, W. J. Briels, *J. Chem. Phys.* **2011**, *135*, 104902.
- [57] I. Santos de Oliveira, W. K. den Otter, W. J. Briels, *Europhys. Lett.* **2013**, *101*, 28002.
- [58] P. Kindt, W. J. Briels, *J. Chem. Phys.* **2007**, *127*, 134901.
- [59] G. Schneider, K. Nusser, S. Neueder, M. Brodech, L. Willner, B. Farago, O. Holderer, W. Briels, D. Richter, *Soft Matter* **2013**, *9*, 4336.
- [60] P. J. Flory, *J. Chem. Phys.* **1942**, *10*, 51.
- [61] M. L. Huggins, *J. Chem. Phys.* **1941**, *9*, 440.
- [62] R. Koningsveld, W. H. Stockmayer, E. Nies, *Polymer Phase Diagrams: A Textbook*, Oxford University Press, Oxford **2001**.
- [63] I. C. Sanchez, R. H. Lacombe, *J. Chem. Phys.* **1976**, *80*, 2352.
- [64] R. Koningsveld, L. Kleintjens, *Macromolecules* **1971**, *4*, 637.
- [65] B. W. Fitzgerald, W. J. Briels, *Macromolecular Theory and Simulations* **2018**, *27*, 1870001.
- [66] R. L. C. Akkermans, W. J. Briels, *J. Chem. Phys.* **2001**, *115*, 6210.
- [67] P. Bolhuis, A. Louis, *Macromolecules* **2002**, *35*, 1860.
- [68] I. M. Ilie, W. J. Briels, W. K. den Otter, *J. Chem. Phys.* **2015**, *142*, 114103.
- [69] G. Heinrich, M. Klüppel, T. A. Vilgis, *Curr. Opin. Solid State Mater. Sci.* **2002**, *6*, 195.
- [70] N. Jouault, F. Dalmás, F. Bouř, J. Jestin, *Polymer* **2012**, *53*, 761.
- [71] J. Domurath, M. Saphiannikova, G. Heinrich, *Macromol. Symp.* **2014**, *338*, 54.
- [72] X. Tan, Y. Zhao, M. Shang, G. R. Hamed, L. Jia, *Polymer* **2017**, *122*, 242.